



# Source characteristics of the 2017 $M_w$ 6.4 Mojabana, Botswana earthquake, a rare lower-crustal event within an ancient zone of weakness

Kathryn Materna<sup>a,\*</sup>, Shengji Wei<sup>b,c</sup>, Xin Wang<sup>b</sup>, Luo Heng<sup>d</sup>, Teng Wang<sup>b</sup>, Weiwen Chen<sup>b</sup>, Rino Salman<sup>b</sup>, Roland Bürgmann<sup>a</sup>

<sup>a</sup> Berkeley Seismology Lab, Berkeley, CA, USA

<sup>b</sup> Earth Observatory of Singapore, Nanyang Technological University, Singapore

<sup>c</sup> Asian School of the Environment, Nanyang Technological University, Singapore

<sup>d</sup> Wuhan University, Wuhan, China

## ARTICLE INFO

### Article history:

Received 4 April 2018

Received in revised form 15 October 2018

Accepted 4 November 2018

Available online xxxx

Editor: J.-P. Avouac

### Keywords:

InSAR–telescismic joint inversion

Sentinel-1

2017 Mojabana earthquake

intraplate earthquake

## ABSTRACT

The 2017 Mojabana earthquake in central Botswana ( $M_w$ 6.4) was a large and deep event for a continental interior and occurred in a region with little historical seismicity. Based on InSAR measurements of surface deformation spanning the event and teleseismic observations, we determine the ruptured fault plane and finite rupture model of the earthquake. Although this oblique normal-faulting earthquake is too deep to uniquely determine the rupture plane geometry from InSAR alone, the best-fitting fault plane constrained by the joint inversion of teleseismic waveforms and InSAR data has a southwest dip and a strike of  $126^\circ$ , roughly consistent with the geologically mapped strike of the Kaapvaal craton's northern edge. Our results indicate that the earthquake had a total duration of  $\sim 10$  s, characterized by two major asperities. The first asperity nucleated in the lower crust and then the rupture propagated up-dip. The lower crustal asperity shows a much shorter rise time compared with the shallower asperity, indicating that contrasts in stress or material properties may have played an important role in the rupture process. The earthquake appears to have occurred in the Limpopo belt, a Proterozoic orogenic belt that represents an ancient zone of weakness between the Archean Zimbabwe and Kaapvaal cratons. In the present day, this zone of weakness may be responding to the stress field imposed by the East African Rift System.

© 2018 Elsevier B.V. All rights reserved.

## 1. Introduction

The vast majority of global seismicity is associated with active faults along plate boundaries. However, the occurrence of intraplate earthquakes demonstrates that continental interiors are not entirely stable and are associated with seismic hazard (England and Jackson, 2011). Large intraplate earthquakes, although rare, show that continental lithosphere can build up significant tectonic or non-tectonic stresses. The causes of these earthquakes have long been debated in the literature (Liu and Zoback, 1997; Pollitz et al., 2001; Calais et al., 2016).

A large intraplate earthquake occurred in a remote area of central Botswana on April 3, 2017. The Mojabana earthquake had an oblique normal faulting mechanism (Fig. 1), nucleated at a depth of 29 km, and had a W-phase moment magnitude of  $M_w$ 6.5

(ANSS ComCat). It was widely felt in Botswana, Zimbabwe, and South Africa. Some buildings in nearby villages sustained structural damage, but there were no reported casualties (Government of Botswana, 2017). The event produced 11  $M_b$ 4–5 aftershocks recorded in the USGS catalog, with the most recent so far occurring in November 2017.

The earthquake occurred in an area with no historic record of seismicity (from the ISC-GEM catalog, dating back to 1920), very little topographic relief, and no known active faults. Before this earthquake occurred, most seismic activity in Botswana was in the Okavango Delta, several hundred kilometers to the north (Reeves, 1972; Gumbrecht et al., 2001). In this study, we jointly analyze Interferometric Synthetic Aperture Radar (InSAR) measurements of deformation from the earthquake and teleseismic waveform observations to constrain the source parameters and kinematic rupture of the event. We also consider geologic and geophysical information on the epicentral area to better understand the event's tectonic framework.

\* Corresponding author.

E-mail address: kmaterna@berkeley.edu (K. Materna).

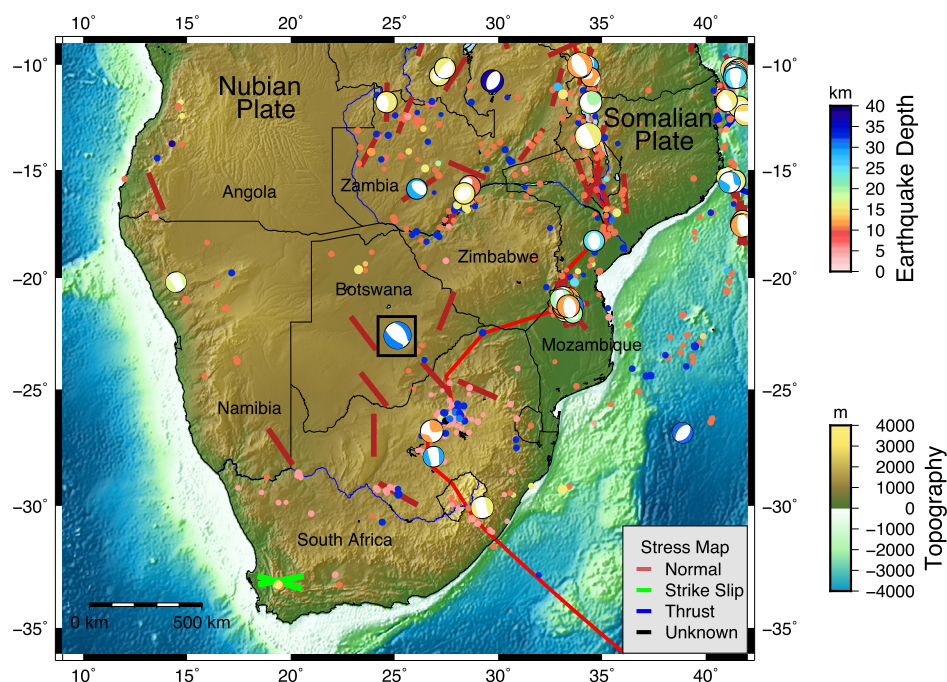


**Fig. 1.** Tectonic setting of southern Africa. The colored dots represent historical earthquakes in the USGS COMCAT catalog (1910–2017). Moment tensors are shown where available in the GCMT catalog from 1976–2017 (Ekström et al., 2012). Event colors represent hypocentral depth from the USGS. The simplified EARS plate boundary from Bird (2003) is shown in red. The 2017 Mojabana earthquake is outlined by a black box. Orientations of  $S_{Hmax}$  from the World Stress Map 2008 (Heidbach et al., 2010) are drawn as solid bars, colored according to their faulting environment. (For interpretation of the colors in the figure(s), the reader is referred to the web version of this article.)

## 2. Tectonic setting

The large-scale active tectonic regime of southern Africa (Fig. 1) is the East African Rift System (EARS). The rift system is accommodating extension between the African plate (Nubia) and the Somalia plate (DeMets et al., 2010). Extension is faster (4–6 mm/yr) in the north and slower (1–2 mm/yr) in the south, where the rift also splits into eastern and western branches (Kinabo et al., 2007; Stamps et al., 2008). In Botswana, the southwestern EARS produces slow extension in the northwest of the country, but is not known to extend to the area of the earthquake.

Southern Africa includes a broad region known as the Kalahari craton (Hanson et al., 2004; Priestley et al., 2006), which contains most of Botswana and the epicenter of the Mojabana earthquake. This craton is generally Archean in age and participated in the formation of multiple supercontinents through geologic time (Groenewald et al., 1995). The Kalahari craton has remained stable over the last 2.3 Ga, although there is evidence for intrusions and orogenesis within the craton at various times (Priestley et al., 2006). At a smaller scale in Botswana, the Kalahari craton is made of a number of constituent geologic terranes (Fig. 2a). Prominently, the Kaapvaal craton and Zimbabwe craton are two major blocks of Archean age that have been deformed little since their formation, and the rocks within these cratons display only low-grade metamorphism (Begg et al., 2009; de Wit et al., 1992).

In contrast, a series of highly deformed Archean and Proterozoic orogenic belts surround these cratonic blocks (Fig. 2). The Limpopo belt is Archean age continental material (de Wit et al., 1992) that was subjected to multiple episodes of intense deformation and high-grade metamorphism throughout the Proterozoic (Mapeo et al., 2001). The southern edge of the Limpopo belt is the Mahalapye belt, a mix of heavily deformed migmatite, gneiss, granodiorite, and quartz-monzonite that is intruded by granitic plutons (Millonig et al., 2010; Ranganai et al., 2002). North and west of the Kaapvaal craton, the Makondi, Okwa, and Kheis belts together comprise a NE-SW trending structure known as the Kalahari Su-

ture Zone (Key and Ayres, 2000). This former thrust zone contains granulite facies metamorphic rocks such as garnet-bearing gneiss (Mapeo et al., 2001), but in many places today is overlain with thick Phanerozoic sediments from the Kalahari desert (Schluter, 2006). The age range for most deformation in the orogenic belts around the two cratons is 1.96–2.06 Ga (Key and Ayres, 2000; Mapeo et al., 2001).

The most recent major deformation event throughout Botswana was the emplacement of the Karoo igneous dykes related to the Mesozoic breakup of Gondwana (Le Gall et al., 2005). A survey of almost 400 Karoo dykes found that they consist of mainly basalt, dolerite, and gabbro, and that 87% of them were emplaced 178–179 Ma (Le Gall et al., 2005). Some of the dykes trend NE while others trend WNW through the Limpopo belt. An aeromagnetic dataset clearly showing the Karoo dyke intrusions is shown in Fig. 2b.

Further north in Botswana, the Damara Belt and Okavango Rift Zone (ORZ) form an ancient collisional zone that now accommodates geologically recent rifting (Kinabo et al., 2007; Modisi et al., 2000). The ORZ, consisting of multiple northeast striking half-grabens, is often considered a type example of an incipient rift, as rift initiation is inferred to be as young as 40 Ka (Bufford et al., 2012; Kinabo et al., 2008). The ORZ is part of the southwest branch of the EARS, but there are no mapped faults or evidence of young tectonism south of  $\sim 21^\circ\text{S}$  (Bufford et al., 2012).

Historical seismicity in southern Africa is primarily related to EARS features, such as the ORZ and rifting in Zimbabwe/Zambia, or related to mining activity in central South Africa (Fig. 1). Two large rifting earthquakes have taken place in recent years: a  $M_w 6.2$  event in Malawi in 1989, and a  $M_w 7.0$  event in Mozambique (Copley et al., 2012). Most present-day seismicity in Botswana, including a sequence of two  $M 5.8$ – $M 5.9$  earthquakes in 1952, is associated with the ORZ (Reeves, 1972; USGS).

Previous work on the Mojabana earthquake has focused on the geologic and aeromagnetic features at the edge of the Kaapvaal craton, the surface deformation patterns, and the potential associ-

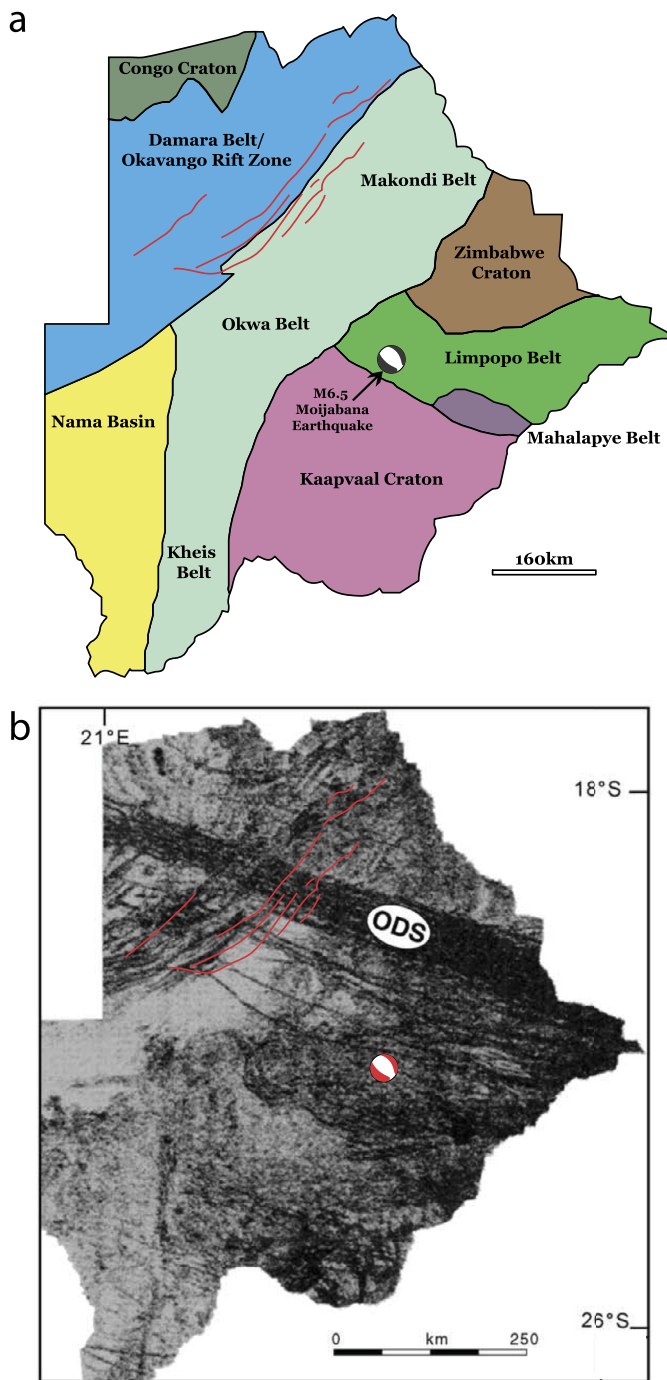


**Fig. 2.** a) Schematic geologic map of Archean terranes in Botswana based on a compilation of maps and information in Key and Ayres (2000), Schluter (2006), Mapeo et al. (2001), and Millonig et al. (2010). b) Aeromagnetic data over Botswana showing the placement of Karoo dykes. Figure is adapted from Le Gall et al. (2005). ODS represents the Okavango Dyke Swarm, a member of the Karoo dykes. Fault traces of the ORZ, shown as red overlays, are from Kinabo et al. (2007).

ation of the event with anthropogenic activity (Albano et al., 2017; Kolawole et al., 2017). In this work, we combine the InSAR-measured surface deformation of the event with teleseismic waveform modeling to better understand the earthquake's source parameters and tectonic setting.

### 3. InSAR data and modeling

We use synthetic aperture radar (SAR) acquisitions from the European Space Agency's Sentinel-1B satellite to quantify the de-

formation field of the Mojabana earthquake. Twenty-one scenes from December 24, 2016 to September 2, 2017 obtained along the ascending orbit were processed to form interferograms. No descending-orbit data have been collected over this area.

We selected the first image acquired before the earthquake as master and co-registered all the other images with it, forming 20 interferograms with the same master image. We used a digital elevation model from the Shuttle Radar Topography Mission (SRTM-1) to correct for the contribution of topographic phase. Phase unwrapping was performed using the statistical-cost network-flow algorithm for phase unwrapping (SNAPHU) (Chen and Zebker, 2000). After unwrapping these interferograms, a linear ramp was estimated from data points far away from the deformed area and was removed from each interferogram in order to account for possible long-wavelength orbit errors and atmospheric noise. We discarded 6 interferograms with visible complex atmospheric turbulence that is difficult to estimate. In order to suppress temporally uncorrelated noise, we then averaged the two sets of remaining unwrapped interferograms: one containing interferograms formed between the master and the images acquired before the earthquake, and the other formed between the master and images acquired after the earthquake (Table S1). We subtracted the averaged unwrapped phase measurements from these two sets of interferograms to obtain a cleaner coseismic deformation measurement. Finally, we used the quadtree downsampling method (Jonsson et al., 2002) to reduce the number of InSAR data to 438 points, making the inversion computations more feasible.

The observations show that the earthquake locations in the USGS COMCAT catalog, the GCMT catalog, and the InSAR data are quite close (within 10 km; Fig. 3), suggesting that location biases from errors in the seismic velocity model are small compared to some other areas (Weston et al., 2011). The USGS hypocentral (29 km) and moment tensor (23 km) depth estimates place the event in the lower crust. Surface displacement patterns for deep faulting events generally have the same nodal-plane ambiguities as seismic moment tensor solutions, and the ambiguity increases with source depth. Our goal in modeling the deformation was to find best-fitting solutions based on both nodal planes and compare their misfit values, in hopes of identifying a preferred fault plane and kinematic slip model from the surface deformation.

With the unwrapped InSAR observations, we performed a non-linear inversion for fault location, geometry and uniform slip amplitude and direction on the fault. We used the Markov Chain Monte Carlo (MCMC) slice-sampling technique from Neal (2003) to draw random samples from the posterior probability density function for each parameter in the model. Initially we prescribed the source to be a rectangular uniform-slip patch with length 23.4 km, width 13.6 km, and slip of 0.66 m. These describe the dimensions for a typical  $M_w$  6.5 normal-faulting rupture (Wells and Copper-smith, 1994). We then used rectangular dislocation elements in an elastic half-space (Okada, 1985) with Poisson's ratio of 0.25 to form Green's functions for line-of-sight (LOS) displacements. We computed the modeled LOS displacements at 438 locations of the down-sampled InSAR observations (Fig. 4).

As this is a blind rupture and we do not have knowledge of fault structures at depth from past seismicity, we allowed for 7 free parameters in the inversion. The parameters of the inversion are strike, dip, rake, the  $x$  and  $y$  coordinates of the upper left corner of the fault plane, fault depth  $z$ , and event moment magnitude (corresponding to a uniform slip value on the prescribed dislocation plane). We began with initial models drawn from the two focal planes in the GCMT moment tensor solution, and placed the top of the fault plane at 23 km depth (strike, dip, rake = 126, 51, -107 and strike, dip, rake = 332, 41, -70). We instituted wide-ranging uniform priors on most parameters. For instance, the range of possible strike values was  $90^\circ$  (i.e., the uniform prior spanned



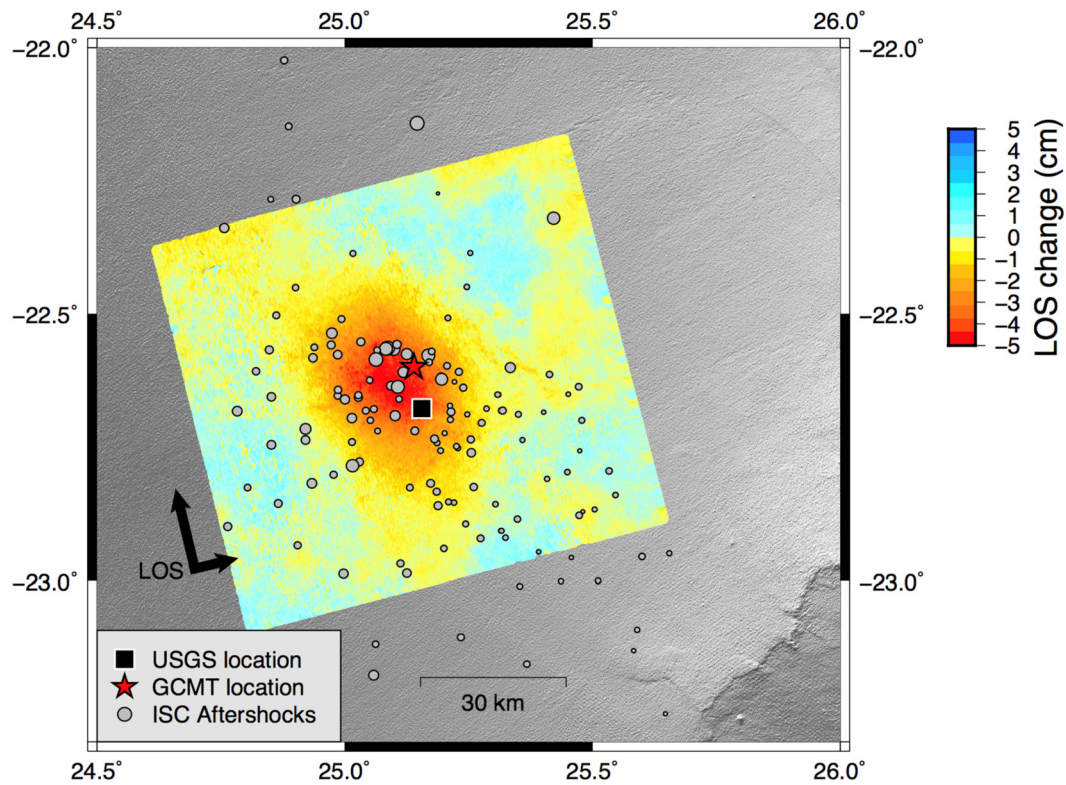


**Fig. 3.** Unwrapped Sentinel-1B stack of interferograms for the Mojabana earthquake. Negative line-of-sight (LOS) displacement means that the ground moves away from the satellite, representing either subsidence or east–northeast movement. Aftershocks are from the ISC catalog (<http://www.isc.ac.uk/iscbulletin/search/catalogue/>).

90°–180° for inversions using the southwest-dipping plane, and 270°–360° for inversions using the northeast-dipping plane). The uniform priors on dip and rake also spanned 90°. The prior distribution on moment magnitude ranged from 6.3 to 6.7. We then initialized models from the two possible nodal planes of the moment tensor, generated 20,000 samples for each model, and analyzed the posterior probability density functions (PDFs).

The nonlinear inversion results show that we are able to fit the downsampled data very well using fault planes in both NE-dipping and SW-dipping orientations. The overall best-fitting model is a NE-dipping plane (Fig. 4) with a strike of 326° and an RMS misfit of 2.2 mm. When we use a SW-dipping plane, our best-fitting model has a strike of 131° and fits the data with a 2.3 mm RMS value (Fig. 5). The PDFs for strike, rake, dip, and position are well constrained in both cases. The best-fitting inversion results for both focal planes slightly reduce the magnitude of the earthquake, preferring values of approximately  $M_w 6.4$  instead of  $M_w 6.5$  (corresponding to a 27% reduction of moment from the USGS W-phase moment tensor estimate of  $6.188 \times 10^{18}$  N-m). The results are similar if we constrain the magnitude to  $M_w 6.5$ , but the RMS misfit is slightly higher (2.9 mm) for the southwest-dipping plane under that constraint.

We performed synthetic tests in order to determine the sensitivity of the InSAR data to the fault plane in question, as both conjugate fault planes seemed to model the data extremely well. As a test, we produced several forward-modeled displacement fields from rectangular sources of known source parameters, added a small amount of Gaussian random noise, and attempted to recover the input sources through our inversion procedure (Table 1). In the first case, we forward modeled a rectangular fault source defined in the “Input Source” column and added Gaussian random noise with an amplitude of 3.0 mm to simulate the typical misfit of our inversions in Figs. 4 and 5. We found that we can reproduce the synthetic displacement field equally well with solutions near both

nodal planes (“Inverted Source” column in Table 1A). The RMS misfit values for inverted solutions based on the two fault planes were identical.

In the case of inverting the forward-modeled displacement field with no additional noise, we still found that we were unable to distinguish the fault plane with the data (Table 1B) because the RMS misfits for the two possible fault planes were very similar. However, repeating the synthetic test with a source at 15 km depth rather than 23 km, we found that the inversion begins to distinguish between the input fault geometry and the conjugate fault geometry (Table 1C) through producing lower misfits for the plane matching the input geometry.

In light of our inversion results and synthetic tests, we suggest that two sets of strike, dip, and rake values satisfy the observed InSAR data within the level of the noise. For an earthquake of this magnitude and depth, InSAR measurements alone may be unable to determine which of the two fault planes ruptured. Additional constraints beyond the InSAR are required to unambiguously resolve the fault plane for an earthquake of this magnitude and depth.

#### 4. Teleseismic data and modeling

In order to provide additional constraints on this earthquake, we performed joint teleseismic-InSAR inversions for the finite fault model of the earthquake. We discretize the planar fault into smaller subfaults, and invert for the slip, rake, rise time, and averaged rupture velocity on each subfault. The seismic data are more sensitive to the time evolution of the rupture, while the geodetic data are more sensitive to the static fault displacements; therefore, the combination of the two datasets may provide stronger constraints on the source parameters.

We downloaded the teleseismic broadband waveform data from an angular distance range of 30°–90° from the IRIS II and IU

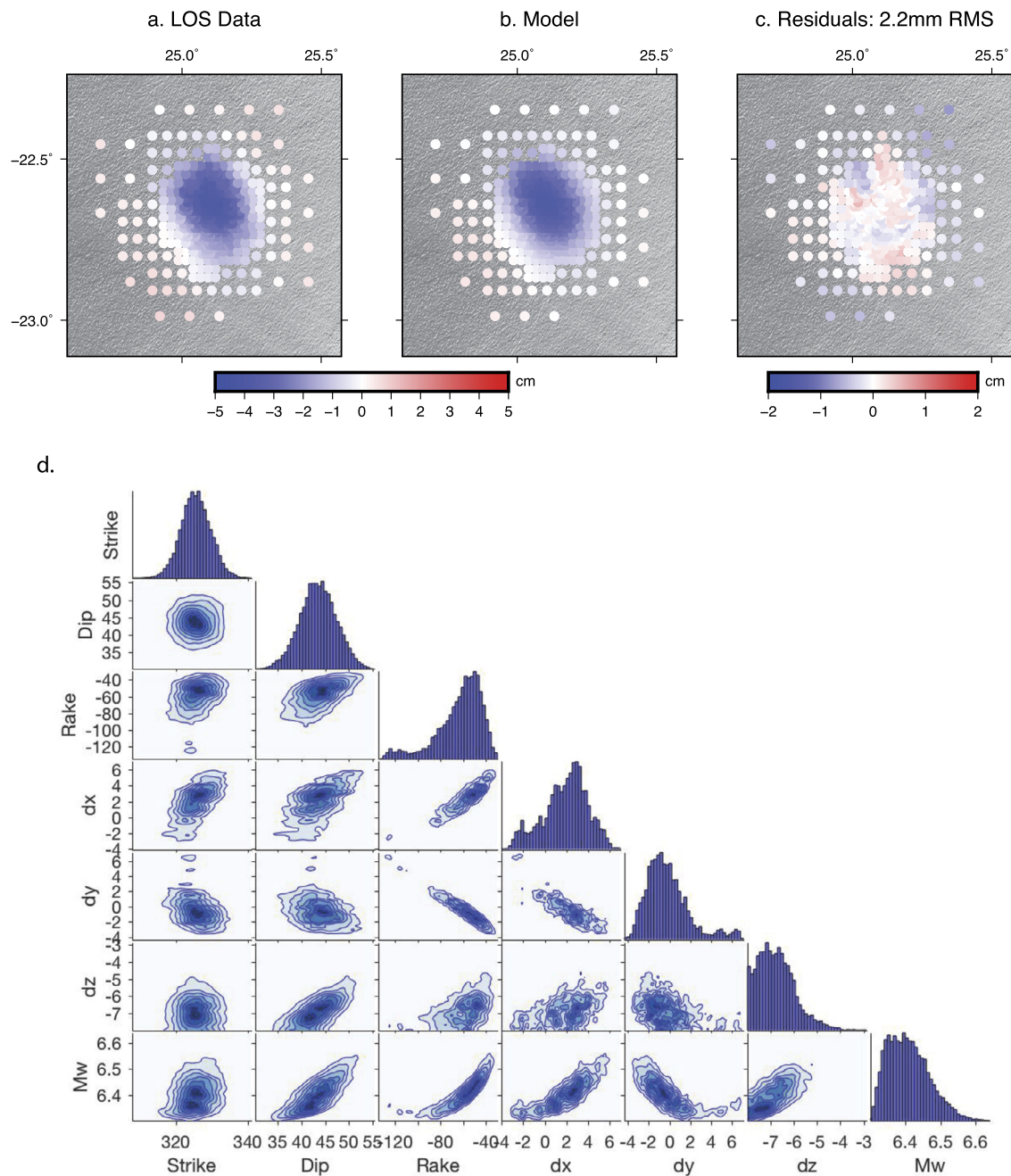


**Fig. 4.** a) Unwrapped and sub-sampled line-of-sight displacement data for the Mojabana earthquake. b) Preferred model based on best-fitting posterior parameter values with a NE-dipping plane (strike = 326°). c) Residuals to the best-fitting model. d) Histograms and tradeoff diagrams showing model parameter distributions from the MCMC sampling algorithm. Positive z is deeper; negative z is shallower.

networks. We selected stations to sample the focal sphere as uniformly as possible. Although there are many high quality stations available, we did not use all of them because nearby stations have very similar P and SH waveforms. Based on these criteria, we selected 39 P-waves and 36 SH-waves to provide good coverage in azimuth and distance (Fig. S1). The instrument response was removed and the displacement waveforms were low-pass filtered below 1 Hz. Synthetic waveforms were produced using a 1D layered earth model with Moho depth constrained from a receiver function study (Nguuri et al., 2001). The same velocity model is used to calculate the static Green's functions with a method proposed by Xie and Yao (1989). We weighted the teleseismic and InSAR datasets equally and imposed a smoothing constraint on the slip distribution in the inversion. The non-linear inversion was solved with a

simulated annealing algorithm to quickly converge on global minima (Ji et al., 2002). Finally, we tried inversions on the candidate nodal fault planes in the GCMT solution at a range of hypocentral depths. We found that a hypocenter of 29 km provides the best fit for both fault planes. We also found that the GCMT solution is similar to the solution when we inverted the P and SH waveforms for a focal mechanism (Text S1, Fig. S9).

The best-fitting joint inversion result was found using a SW-dipping fault plane (strike = 126°; Fig. 6). Both the modeled teleseismic waveforms and InSAR results fit the data well (Fig. 6 and Fig. 7). The displacement P-waves and the depth phases (pP and sP) show clear multiple asperities, indicating a complex rupture process of the earthquake. The best-fitting model shows a rupture that initiated at ~30 km depth in the lower crust and propagated

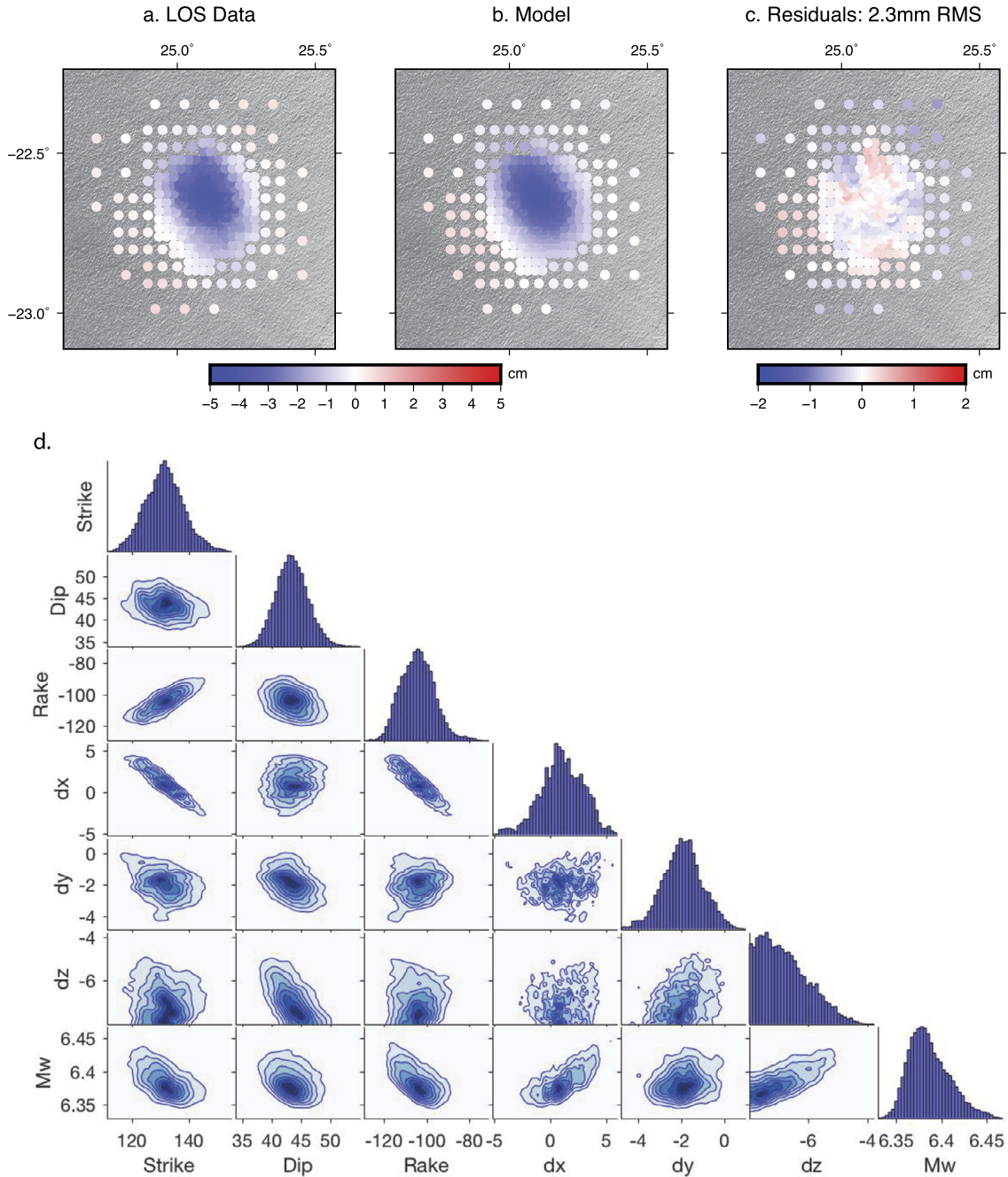


**Fig. 5.** Same as Fig. 4 for the southwest dipping plane (strike = 126°).

updip to ~20 km deep, where it resulted in about 80 cm of slip at the peak of the slip distribution (Fig. 6). The modeled moment magnitude reflects a  $M_w$  6.4 event, slightly smaller than the  $M_w$  6.5 reported in the W-phase moment tensor. The depth distribution is consistent with the reported hypocenter of 29 km and centroid depth of 23 km. The deep asperity shows a shorter rise time (~1 s) compared with the shallower rupture (>2 s), corresponding to two peaks in the moment rate function (Fig. 6c). However, we note that the constraint on the risetime from teleseismic waveform data is relatively weak, and that additional nearfield strong motion data, if there is any, is needed to better resolve the risetime. The inversion results on northeast-striking planes produced clearly worse fits to the teleseismic data than the results using southwest-striking planes (average waveform cross-correlation co-

efficients of 84.8% vs. 81.1%), especially for the depth phases (Fig. 7, Figs. S2–S3).

Compared to the joint inversions, teleseismic-only inversions show similar first-order slip dimensions and peak slip (Figs. S4–S5). However, the inversions differ in the relative strength of the two asperities in Fig. 6. The teleseismic-only inversion has a stronger asperity on the deeper part of the fault plane and a weaker asperity on the shallow part (Fig. S4a). This discrepancy makes sense given that the deeper asperity also has a shorter rise time in the joint inversion, thus contributing more to the seismic signal.

To verify the ruptured fault plane (southwest dipping) as revealed by the joint inversion of teleseismic and InSAR data, we further refined the location and focal mechanisms of three aftershocks, aiming at delineating the fault geometry. The procedure uses regional broadband waveforms to determine the aftershock



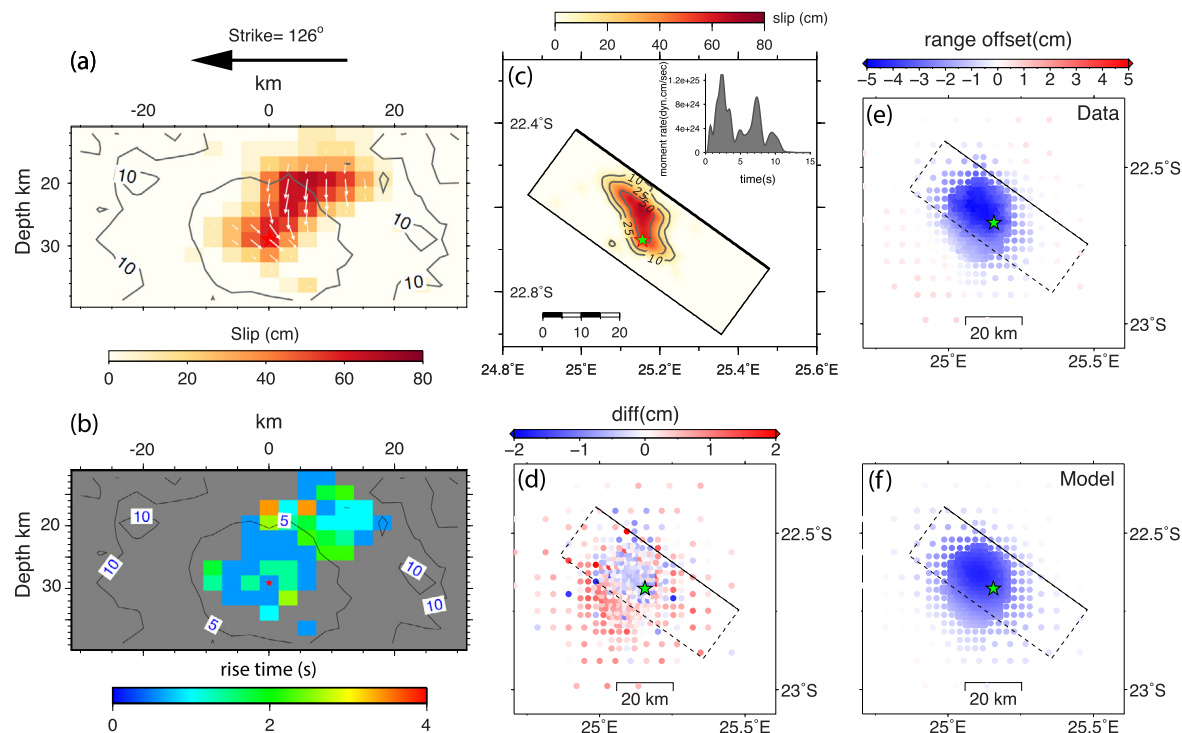


**Fig. 6.** Joint teleseismic-InSAR inversion results for a plane with 126° strike. a) Solution for distributed slip on the fault interface. b) Distribution of rise time on the interface. c) Map view of slip distribution, and moment rate function produced by the inversion. d) Residuals between InSAR LOS data and model. e) InSAR LOS data. f) Model fit to the InSAR LOS data (RMS misfit = 6.3 mm).

**Table 1**  
Synthetic tests for resolving the geometry of a known source through the nonlinear inversion technique. The two inversion results for each input source correspond to starting models of either nodal plane geometry.

Input source (strike/dip/rake)	Input depth (km)	Applied noise (mm)	Inverted source (strike/dip/rake)	RMS misfit (mm)
A. 126, 51, −107	23	3	129, 50, −105	3.0
A. 126, 51, −107	23	3	325, 38, −64	3.0
A. 332, 41, −70	23	3	129, 50, −105	2.9
A. 332, 41, −70	23	3	326, 42, −88	3.0
B. 126, 51, −107	23	0	130, 52, −105	0.7
B. 126, 51, −107	23	0	330, 36, −59	0.5
B. 332, 41, −70	23	0	139, 47, −100	0.6
B. 332, 41, −70	23	0	332, 42, −74	0.5
C. 126, 51, −107	15	0	127, 51, 107	0.4
C. 126, 51, −107	15	0	321, 37, −65	1.3
C. 332, 41, −70	15	0	146, 45, −94	1.3
C. 332, 41, −70	15	0	331, 42, −76	0.6

focal mechanisms, and then refines their horizontal locations relative to the mainshock by surface wave cross-correlation. Finally, the depths of the aftershocks were constrained by modeling of teleseismic depth phases. The methods we employed are similar to those described in Wang et al. (2017, 2018), and Zhu and Helmberger (1996). See supplemental material and Figs. S9–S14 for more details. Our refined aftershock distribution (Fig. 8), although it only includes three aftershocks, delineates a fault plane that is dipping to the southwest, consistent with our joint inversion results.

5. Discussion

The  $M_w$ 6.4 Mojabana earthquake in central Botswana was a large earthquake for a location far away from known plate boundaries. Stable continental regions, such as the epicentral region of this earthquake, are thought to generate only 0.3% of seismic mo-

ment release globally (Johnston, 1989). As such, it is important to understand this rare event’s tectonic and geodynamic context. Here we interpret the findings of the InSAR and teleseismic modeling, and discuss the region’s tectonic setting and potential stress conditions.

5.1. Geophysical inversion results

Our modeling of the InSAR dataset for source fault parameters reveals slightly lower RMS misfit values on planes that dip to the northeast, consistent with previous analyses of this event (Albano et al., 2017; Kolawole et al., 2017). However, we find that due to the depth of the earthquake, the magnitude, and the single viewing geometry available from the Sentinel-1B satellite, we can model the LOS observations almost equally well with models from both possible fault orientations. This conclusion is similar to that of Gardonio et al. (2018), who also analyze Sentinel-1 In-

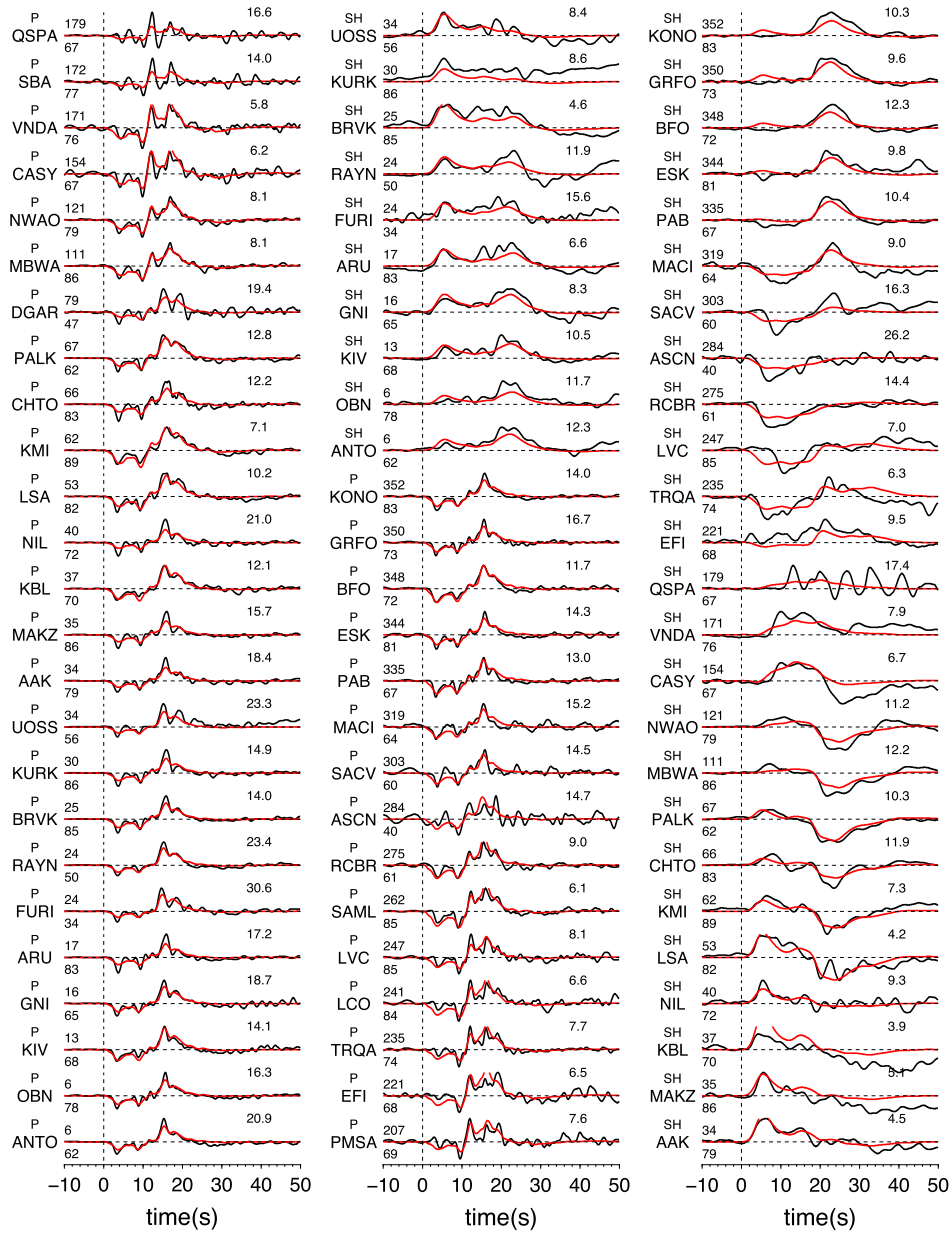


**Fig. 7.** Telesismic waveform fits for P and SH phases from the joint telesismic-InSAR inversion of the Mojabana earthquake. The numbers above and below the start of each trace represent the azimuth to the station and the station angular distance in degrees, respectively. The numbers on the top right of each trace are the peak amplitudes of the data in micrometers. The average waveform cross-correlation coefficient between data and synthetics is 84.8%.

SAR data and obtain a similarly ambiguous result with respect to the modeled fault plane. We note that the preferred fault models of our study and Gardonio et al. (2018) differ in the details, and in particular, the fault dip differs by as much as 30 degrees. We suspect that differences in modeling strategies can explain these discrepancies. InSAR downsampling, atmospheric noise mitigation, inclusion of rake as a free parameter, and data covariance assumptions are all different between the two studies, and we suspect that such differences can influence the results of the inversions. Another difference could be the time span of data used. For our inversion, we use a months-long stack of InSAR images, which may include some postseismic signal (Table S1). However, we do not see evidence for resolvable postseismic deformation in interferograms from 0–5 months after the earthquake (Fig. S9), so we think this effect is small. Instead, these differences likely highlight the inherent challenges of using geodetic-only data to resolve the precise kinematics of deep earthquakes.

We find that the joint InSAR-telesismic dataset, on the other hand, is better able to resolve the focal plane ambiguity, as has been observed for other earthquakes around the world (Weston et al., 2014). As the two conjugate fault planes of the moment tensor solution are equivalent in the double couple point source solution, they will produce identical waveform synthetics if the source is simple enough to be approximated by a point source. The waveforms of this event, and in particular the P-waves, require a finite rupture model with multiple asperities and rupture directivity to better represent the complexity of the source. In this case, the ambiguity between the two conjugate fault planes can be resolved through the telesismic data. Our modeling results (Figs. 6, 7, S2, and S3) show that the fault plane with a strike of  $126^\circ$  can fit both direct phases and depth phases better than the fault plane with a northwesterly strike. This is also consistent with the relocated epicenters of three aftershocks (Fig. 8).



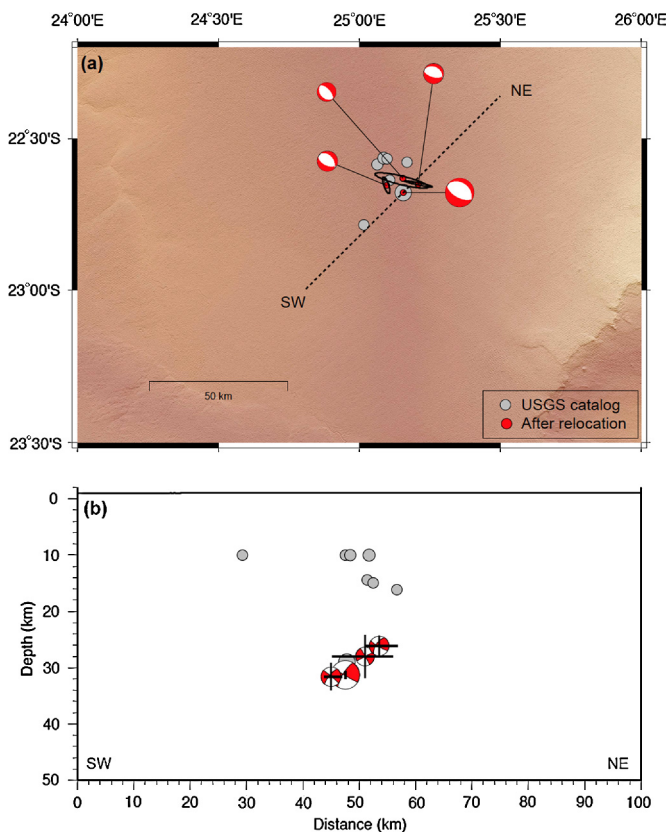


**Fig. 8.** Map view and depth profile of the mainshock and three relocated aftershocks, shown as red dots in the map view and beach balls on the profile. Crosses indicate location uncertainty. For comparison, the earthquake locations from the USGS catalog are shown as gray circles. See supplement for more details.

Both our InSAR-only results and our joint inversion results suggest that the true magnitude of the event may be slightly lower than  $M_w 6.5$ . The InSAR inversions based on both conjugate fault planes find preferred moment magnitude values around 6.4. The preferred models from the joint inversions also result in an event with  $M_w = 6.4$ , a moment reduction of about 27% compared to the moment of the USGS W-phase moment tensor. Similar discrepancies in moment release have been identified in other cases around the world; a global survey found that typical variability of seismic and geodetic moment estimates is about 20%, and can be as high as 44% in some cases (Weston et al., 2011). In the case of the Mojabana earthquake, we speculate that this difference in calculated magnitude may be due to higher-than-average shear modulus at the depth of the earthquake. For the seismic dataset, the high quality of waveform fits for such a relatively small earthquake may result from the simple crustal structure and flat topography in the epicentral region.

The teleseismic dataset also contains an interesting feature with respect to the temporal evolution of this earthquake. The moment rate function shows two distinct peaks, a feature also seen in the SCARDEC solution for the event (Vallee et al., 2011). In the finite source inversion, it seems that the deeper portion of the fault, which ruptured first, had a short rise time ( $< 1$  s), in contrast with a longer rise time ( $> 2$  s) for the shallower portion of the rupture, although near-field data would be needed to fully quantify these rise times. These features of the rupture may indicate that the fault contains a heterogeneous structure of asperities with locally differing stress conditions or frictional properties. Based on our joint inversion slip model, the static stress drop of the earthquake is only around 1 MPa, which is much smaller than the stress drops of most intra-plate earthquakes (Kanamori and Anderson, 1975). Low

stress drops indicate relatively modest high frequency radiation, but unfortunately, we do not have the near field strong motion data that would be needed to verify this.

## 5.2. Deep intraplate events at craton edges

The Mojabana earthquake took place within the Limpopo Belt, a Proterozoic orogenic zone that was previously reactivated during major tectonic episodes. It appears to be located near the contact between the Limpopo Belt and the Kaapvaal craton (Fig. 2a). The Jurassic-age Karoo dyke swarm, emplaced in a nearby area during the break-up of Gondwana, also appears to be associated with the same preexisting zone of weakness (Fig. 2b). The most recent nearby active deformation is found in the Okavango Rift Zone, approximately 300 km to the north.

With a hypocenter at approximately 29 km depth, this earthquake is unusually deep for a rifting event. Receiver functions suggest that the Moho depth in the epicentral region is approximately 45 km (Nguuri et al., 2001), placing this earthquake in the lower crust and upper mantle of southern Africa (Yang and Chen, 2010), suggesting that these regions can support high differential stresses despite high temperatures. Alternatively or in addition, the large depth of the Mojabana earthquake may be related to its location along the edge of the Kaapvaal craton. There is evidence that Proterozoic fold belts at the edges of cratons often host intraplate earthquakes (Mooney et al., 2012), and Craig et al. (2011) show that the deepest rifting earthquakes in southern Africa tend to concentrate along the edges of ancient cratons. In body wave and surface wave seismic tomography, these cratons show high-velocity lithospheric roots, assumed to represent lower temperature material in the upper mantle (James et al., 2001; Priestley et al., 2006). Furthermore, heat flow measurements depict low heat flow values within the Kaapvaal craton and larger values moving away from the craton margin (Ballard et al., 1987). These observations support the notion that the cratons in southern Africa are strong, conductively cooled rock masses that have lower geotherms and locally deepen the maximum depth of the seismogenic portion of the lithosphere (Chen and Molnar, 1983).

While of lower magnitude, several historical earthquakes in this type of setting show close resemblance to this event. Two unusual normal-faulting earthquakes with magnitudes of M4.5 and M3.6 occurred in south-central Sweden in 1986. Much like the Mojabana earthquake, they occurred at 20–35 km deep within a Proterozoic shear zone separating two cratonic blocks, and the strikes of the nodal planes were parallel to the overall strike of the shear zone (Arvidsson et al., 1992). Similarly, the M5.4 Norseman and M5.2 Ravensthorpe earthquakes in southwestern Australia occurred as a result of normal faulting within a Proterozoic mobile belt on the boundary of an Archean craton, even though the overall stress regime in Australia is compressive (Clark, 2004). The Ravensthorpe event is thought to have a focal depth of 19 km (Clark, 2004). It is clear from earthquake catalogs that some stable continental regions are more likely than others to produce bimodal depth distributions with peaks of activity in the lower crust (Klose and Seeber, 2007). However, it appears that intraplate earthquakes in the depth and magnitude range of the Mojabana earthquake are quite rare (Figs. S7a–b, S8; Engdahl et al., 1998).

## 5.3. Possible sources of intraplate stress in southern Africa

The sources of stress that drive intraplate earthquakes are sometimes enigmatic. Plate boundary stresses from distant interfaces are thought to contribute to stress conditions in plate interiors (M. Lou Zoback, 1992). In this case, the EARS may be contributing to stress conditions in central Botswana, even though the area

is ~300 km south of an actively rifting region (Fig. 2). It is possible that the Mojabana earthquake points to the continuing southward propagation of the EARS (Bird et al., 2006), as is occurring in the Okavango Rift Zone in northern Botswana (Kinabo et al., 2007). If this event represents an incipient rift process, then the recurrence interval for this type of earthquake is likely in the thousands of years given the slow geodetic rates of opening in the southern EARS (Stamps et al., 2008). Other possible stressing mechanisms that have been suggested for intraplate earthquakes in general, and which may be related to the earthquakes in Botswana, include gradients in gravitational potential energy (Stamps et al., 2014) and density variations due to subsurface rift pillows (Zoback and Richardson, 1996).

It is also possible that this earthquake represents a response to a geologically recent non-tectonic stress or strength perturbation (Calais et al., 2016). Redistribution of sediments at the Earth's surface, glacial isostatic adjustment and recent thermal weakening have been proposed as stressing mechanisms for other intraplate earthquakes, such as earthquakes in the Okavango Delta and the New Madrid earthquakes in the central United States (Calais et al., 2010; Gumbrecht et al., 2001; Liu and Zoback, 1997; Pollitz et al., 2001). It is difficult to clearly identify which stressing mechanisms could have ultimately brought the fault to failure in this earthquake.

Reliable in-situ measurements of stress are key to understanding the processes behind the Mojabana earthquake, but are rare in Botswana. The few available measurements suggest a stress state consistent with the earthquake's focal mechanism. Three over-coring measurements from mines were reported in Botswana in the World Stress Map 2008, including one close to the earthquake epicenter (Fig. 1). This measurement shows the maximum horizontal stress well aligned with the stress field required to cause the earthquake (Heidbach et al., 2010). However, due to the large errors in over-coring measurements and difficulty verifying the details of the measurement procedure, the stress measurements in Botswana were down-graded to E-quality for the World Stress Map 2016 (Oliver Heidbach, personal communication, 2017), and replacement measurements have not been conducted. Models of deviatoric stresses in Africa, driven by gravitational potential energy from topography and crustal density variations, and geodetic motions also show general east–west tension in Botswana (Stamps et al., 2014). Further observational and theoretical constraints on the stress state are needed to provide a more detailed view of the stresses and associated deformation in this region.

Regardless of the original source of stress, a concentrated strain response in reactivated zones of weakness has long been considered as a possible contributor to the occurrence of intraplate earthquakes (e.g., Hinze et al., 1988), and may be at play in the case of the Mojabana earthquake (Kolawole et al., 2017). The concept has been applied to specific earthquakes such as the New Madrid earthquake sequence (Kenner and Segall, 2000; Pollitz et al., 2001), and has been proposed as a mechanism for persistent weakness of craton margins during supercontinent cycles (Audet and Bürgmann, 2011; Lenardic et al., 2000). We suggest that in the stress field imposed by the southward-propagating EARS and the regional stresses in southern Africa, the fault structures of the Proterozoic Limpopo orogen can accommodate strain between two more rigid cratonic blocks. This earthquake shows that Archean-age fabrics and geologic boundaries, when subject to a present-day stress field, are an important controlling factor for continental deformation (Begg et al., 2009).

## 6. Conclusion

The 3 April 2017 M6.4 Mojabana earthquake in central Botswana, with an unusually large magnitude and at a large depth,

occurred in a region considered a stable continental interior. In order to study this earthquake and its tectonic setting, we compiled existing geophysical and geologic information and modeled the source parameters of the earthquake. We generated a stack of 20 Sentinel-1B InSAR interferograms over the source area. Using this ascending-orbit only dataset, we performed a 7-parameter inversion for strike, dip, rake, magnitude, and three location parameters of the earthquake source. We found that rupture planes close to either focal mechanism nodal plane were able to fit the data within expected noise levels because of the earthquake depth. We performed a joint finite source inversion with InSAR and teleseismic data and found that the teleseismic waveform data favor a fault plane that dips to the southwest, consistent with aftershock relocations. On the basis of geologic studies in the area and analogous intraplate earthquakes elsewhere, we suggest that the earthquake took place within a pre-existing zone of weakness from a Proterozoic collisional episode between two cratonic blocks. Future studies of the geology, geophysical data, and aftershock patterns may be helpful in further illuminating the geometry and long-term behavior of the fault that ruptured in the event.

## Acknowledgements

Copernicus Sentinel-1 data (2017) were provided by the European Space Agency and downloaded through the Alaska Satellite Facility (<https://www.asf.alaska.edu>). Earthquake data and felt reports were extracted from the USGS webpage and the USGS COMCAT database (<http://earthquake.usgs.gov/>). Moment tensors were drawn from the Global Centroid Moment Tensor (GCMT) database (<http://www.globalcmt.org/CMTsearch.html>). Seismic waveform data were downloaded from IRIS for the II and IU networks (<https://dx.doi.org/10.7914/SN/IU>, <https://dx.doi.org/10.7914/SN/II>). Maps were made using GMT. K.M. is supported through the National Science Foundation Graduate Research Fellowship Program, Award # 1752814. S.W. and X. W. are supported by research grant (M4430239) from Earth Observatory of Singapore. The authors are grateful to Emma Hill, Doug Dreger, Christopher Johnson, and Eric Lindsey for helpful comments. The authors also thank two anonymous reviewers and the editor for their comments that improved the manuscript.

## Appendix A. Supplementary material

Supplementary material related to this article can be found online at <https://doi.org/10.1016/j.epsl.2018.11.007>.

## References

- Albano, M., Polcar, M., Bignami, C., Moro, M., Saroli, M., Stramondo, S., 2017. Did anthropogenic activities trigger the 3 April 2017. *Remote Sens.* 9 (1028), 1–12. <https://doi.org/10.3390/rs9101028>.
- Arvidsson, R., Wahlstrom, R., Kulhanek, O., 1992. Deep-crustal earthquakes in the southern Baltic Shield. *Geophys. J. Int.* 108, 767–777.
- Audet, P., Bürgmann, R., 2011. Dominant role of tectonic inheritance in supercontinent cycles. *Nat. Geosci.* 4 (3), 184–187. <https://doi.org/10.1038/ngeo1080>.
- Ballard, S., Pollack, H.N., Skinner, N.J., 1987. Terrestrial heat-flow in Botswana and Namibia. *J. Geophys. Res.* 92 (B7), 6291–6300. <https://doi.org/10.1029/JB092iB07p06291>.
- Begg, G.C., Natapov, L.M., Reilly, S.Y.O., Neill, C.J.O., Bowden, P., 2009. The lithospheric architecture of Africa: seismic tomography, mantle petrology, and tectonic evolution. *Geosphere* 5 (1), 23–50. <https://doi.org/10.1130/GES00179.1>.
- Bird, P., 2003. An updated digital model of plate boundaries. *Geochem. Geophys. Geosyst.* 4 (3). <https://doi.org/10.1029/2001GC000252>.
- Bird, P., Ben-avraham, Z., Schubert, G., Andreoli, M., Viola, G., 2006. Patterns of stress and strain rate in southern Africa. *J. Geophys. Res.* 111 (February), 1–14. <https://doi.org/10.1029/2005JB003882>.
- Bufford, K.M., Atekwana, E.A., Abdelsalam, M.G., Shemang, E., Atekwana, E.A., Mickus, K., Moidaki, M., Modisi, M.P., Molwalefhe, L., 2012. Geometry and faults tectonic activity of the Okavango Rift Zone, Botswana: evidence from magnetotelluric and electrical resistivity tomography imaging. *J. Afr. Earth Sci.* 65, 61–71. <https://doi.org/10.1016/j.jafrearsci.2012.01.004>.

- Calais, E., Camelbeeck, T., Stein, S., Liu, M., Craig, T.J., 2016. A new paradigm for large earthquakes in stable continental plate interiors. *Geophys. Res. Lett.* 43 (20), 10,621–10,637. <https://doi.org/10.1002/2016GL070815>.
- Calais, E., Freed, A.M., Van Arsdale, R., Stein, S., 2010. Triggering of New Madrid seismicity by late-Pleistocene erosion. *Nature* 466 (7306), 608–611. <https://doi.org/10.1038/nature09258>.
- Chen, C.W., Zebker, H.A., 2000. Network approaches to two-dimensional phase unwrapping: intractability and two new algorithms: erratum. *J. Opt. Soc. Am. A* 17 (3), 401–414. Retrieved from <https://www.osapublishing.org/abstract.cfm?URI=josa-18-5-1192>.
- Chen, W.-P., Molnar, P., 1983. Focal depths of intracontinental and intraplate earthquakes and their implications for the thermal and mechanical properties of the lithosphere. *J. Geophys. Res.* 88, 4183–4214.
- Clark, D., 2004. Seismicity along the northern foreland of the Albany–Fraser Orogen. Available at: [https://www.researchgate.net/profile/Dan\\_Clark3/publication/270822833\\_Seismicity\\_along\\_the\\_northern\\_foreland\\_of\\_the\\_Albania-Fraser\\_Orogen/links/54b59d100cf2318f09a0219/Seismicity-along-the-northern-foreland-of-the-Albania-Fraser-Orogen.pdf](https://www.researchgate.net/profile/Dan_Clark3/publication/270822833_Seismicity_along_the_northern_foreland_of_the_Albania-Fraser_Orogen/links/54b59d100cf2318f09a0219/Seismicity-along-the-northern-foreland-of-the-Albania-Fraser-Orogen.pdf).
- Copley, A., Hollingsworth, J., Bergman, E., 2012. Constraints on fault and lithosphere rheology from the coseismic slip and postseismic afterslip of the 2006  $M_w$  7.0 Mozambique earthquake. *J. Geophys. Res., Solid Earth* 117 (3), 1–16. <https://doi.org/10.1029/2011JB008580>.
- Craig, T.J., Jackson, J.A., Priestley, K., McKenzie, D., 2011. Earthquake distribution patterns in Africa: their relationship to variations in lithospheric and geological structure, and their rheological implications. *Geophys. J. Int.* 185 (1), 403–434. <https://doi.org/10.1111/j.1365-246X.2011.04950.x>.
- de Wit, M.J., de Ronde, C.E.J., Tredoux, M., Roering, C., Hart, R.J., Armstrong, R.A., Green, R.W.E., Peberdy, E., Hart, R.A., 1992. Formation of an Archaean continent. *Nature* 357 (6379), 553–562. <https://doi.org/10.1038/357553a0>.
- DeMets, C., Gordon, R.G., Argus, D.F., 2010. Geologically current plate motions. *Geophys. J. Int.* 181 (1), 1–80. <https://doi.org/10.1111/j.1365-246X.2009.04491.x>.
- Ekström, G., Nettles, M., Dziewoński, A.M., 2012. The global CMT project 2004–2010: centroid-moment tensors for 13,017 earthquakes. *Phys. Earth Planet. Inter.* 200–201, 1–9. <https://doi.org/10.1016/j.pepi.2012.04.002>.
- England, P., Jackson, J., 2011. Uncharted seismic risk. *Nat. Geosci.* 4 (6), 348–349. <https://doi.org/10.1038/ngeo1168>.
- Gardonio, B., Jolivet, R., Calais, E., Leclerc, H., 2018. The April 2017  $M_w$  6.5 Botswana earthquake: an intraplate event triggered by deep fluids. *Geophys. Res. Lett.*
- Government of Botswana (BWGovernment), 2017. This is one of houses damaged by the 6.5 magnitude earthquake in Moiyabana village on Monday. No casualties reported. 5 April 2017, 12:02AM. Tweet: <https://twitter.com/bwgovernment/status/849517666935205890>.
- Groenewald, P.B., Moyes, A.B., Grantham, G.H., Krynauw, J.R., 1995. East Antarctic crustal evolution: geological constraints and modelling in western Dronning Maud Land. *Precambrian Res.* 75 (3–4), 231–250. [https://doi.org/10.1016/0301-9268\(95\)80008-6](https://doi.org/10.1016/0301-9268(95)80008-6).
- Gumbrecht, T., McCarthy, T.S., Merry, C.L., 2001. The topography of the Okavango Delta, Botswana, and its tectonic and sedimentological implications. *S. Afr. J. Geol.* 104, 243–264.
- Hanson, R.E., Crowley, J.L., Bowring, S.A., Ramezani, J., Gose, W.A., Dalziel, I.W.D., Pancake, J.A., Seidel, E.K., Blenkinsop, T.G., Mukwakwami, J., 2004. Coeval large-scale magmatism in cratons during Rodinia assembly. *Science* 304 (May), 1126–1129.
- Heidbach, O., Tingay, M., Barth, A., Reinecker, J., Kurfey, D., Muller, B., 2010. Global crustal stress pattern based on the World Stress Map database release 2008. *Tectonophysics* 482, 3–15.
- Hinze, W.J., Braille, L.W., Keller, G.R., Lidiak, E.G., 1988. Models for midcontinent tectonism: an update. *Rev. Geophys.* 26 (4), 699–717. <https://doi.org/10.1029/RG026i004p00699>.
- James, D.E., Fouch, M.J., VanDecar, J.C., van der Lee, S., Kaapvaal Seismic Group, 2001. Tectospheric structure beneath southern Africa. *Geophys. Res. Lett.* 28 (13), 2485–2488. <https://doi.org/10.1029/2000GL012578>.
- Ji, C., Wald, D.J., Helmburger, D.V., 2002. Source description of the 1999 Hector Mine, California, earthquake, part I: wavelet domain inversion theory and resolution analysis. *Bull. Seismol. Soc. Am.* 92 (4), 1192–1207. <https://doi.org/10.1785/0120000916>.
- Johnston, A.C., 1989. The seismicity of “stable continental interiors”. In: *Earthquakes at North-Atlantic Passive Margins: Neotectonics and Postglacial Rebound*, pp. 299–327.
- Jonsson, S., Zebker, H., Segall, P., Amelung, F., 2002. Fault slip distribution of the 1999  $M_w$  7.1 Hector Mine, California, earthquake, estimated from satellite radar and GPS measurements. *Bull. Seismol. Soc. Am.* 92 (4), 1377–1389.
- Kanamori, H., Anderson, D., 1975. Theoretical basis of some empirical relations in seismology. *Bull. Seismol. Soc. Am.* 65 (5), 1073–1095.
- Kenner, S.J., Segall, P., 2000. A mechanical model for intraplate earthquakes: application to the New Madrid Seismic Zone. *Science* 289 (5488), 2329–2332. <https://doi.org/10.1126/science.289.5488.2329>.
- Key, R.M., Ayres, N., 2000. The 1998 edition of the National Geological Map of Botswana. *J. Afr. Earth Sci.* 30 (3), 427–451. [https://doi.org/10.1016/S0899-5362\(00\)00030-0](https://doi.org/10.1016/S0899-5362(00)00030-0).
- Kinabo, B.D., Atekwana, E.A., Hogan, J.P., Modisi, M.P., Wheaton, D.D., Kampunzu, A.B., 2007. Early structural development of the Okavango rift zone, NW Botswana. *J. Afr. Earth Sci.* 48 (2–3), 125–136. <https://doi.org/10.1016/j.jafrearsci.2007.02.005>.
- Kinabo, B.D., Hogan, J.P., Atekwana, E.A., Abdelsalam, M.G., Modisi, M.P., 2008. Fault growth and propagation during incipient continental rifting: insight from a combined aeromagnetic and Shuttle Radar Topography Mission digital elevation model investigation of the Okavango Rift Zone, northwest Botswana. *Tectonics* 27 (3), 1–16. <https://doi.org/10.1029/2007TC002154>.
- Klose, C.D., Seiber, L., 2007. Shallow seismicity in stable continental regions. *Seismol. Res. Lett.* 78 (5), 554–562. <https://doi.org/10.1785/gssrl.78.5.554>.
- Kolawole, F., Atekwana, E.A., Malloy, S., Stamps, D.S., Grandin, R., Abdelsalam, M.G., ..., Shemang, E.M., 2017. Aeromagnetic, gravity, and Differential Interferometric Synthetic Aperture Radar analyses reveal the causative fault of the 3 April 2017  $M_w$  6.5 Moiyabana, Botswana, earthquake. *Geophys. Res. Lett.* 44, 1–10. <https://doi.org/10.1002/2017GL074620>.
- Le Gall, B., Tshoso, G., Dymont, J., Basira Kampunzu, A., Jourdan, F., Féraud, G., Bertrand, H., Aubourg, C., Vétel, W., 2005. The Okavango giant mafic dyke swarm (NE Botswana): its structural significance within the Karoo Large Igneous Province. *J. Struct. Geol.* 27 (12), 2234–2255. <https://doi.org/10.1016/j.jsg.2005.07.004>.
- Lenardic, A., Moresi, L., Muhlhaus, H., 2000. The role of mobile belts for the longevity of deep cratonic lithosphere: the crumple zone model. *Geophys. Res. Lett.* 27 (8), 1235–1238.
- Liu, L., Zoback, M.D., 1997. Lithospheric strength and intraplate seismicity in the New Madrid Seismic Zone. *Tectonics* 16 (4), 585–595.
- Mapeo, R.B.M., Armstrong, R.A., Kampunzu, A.B., 2001. SHRIMP U–Pb zircon geochronology of gneisses from the Gweta borehole, northeast Botswana: implications for the Palaeoproterozoic Magondi Belt in southern Africa. *Geol. Mag.* 138 (3), 299–308. <https://doi.org/10.1017/S001675680100526X>.
- Millonig, L., Zeh, A., Gerdes, A., Klemd, R., Barton, J.M., 2010. Decompressional heating of the Mahalapye Complex (Limpopo Belt, Botswana): a response to Palaeoproterozoic magmatic underplating? *J. Petrol.* 51 (3), 703–729. <https://doi.org/10.1093/petrology/egp097>.
- Modisi, M.P., Atekwana, E.A., Kampunzu, A.B., Ngwisanyi, T.H., 2000. Rift kinematics during the incipient stages of continental extension: evidence the nascent Okavango rift basin, Northwest Botswana. *Geology* 28 (10), 939–942. [https://doi.org/10.1130/0091-7613\(2000\)28<939:RKDTIS>2.0.CO;2](https://doi.org/10.1130/0091-7613(2000)28<939:RKDTIS>2.0.CO;2).
- Mooney, W.D., Ritsema, J., Keun, Y., 2012. Crustal seismicity and the earthquake catalog maximum moment magnitude ( $M_{max}$ ) in stable continental regions (SCRs): correlation with the seismic velocity of the lithosphere. *Earth Planet. Sci. Lett.* 357–358, 78–83. <https://doi.org/10.1016/j.epsl.2012.08.032>.
- Neal, R., 2003. Slice sampling. *Ann. Stat.* 31 (3), 705–741.
- Nguiri, T.K., Gore, J., James, D.E., Webb, S.J., Wright, C., Zengeni, T.G., Gwavava, O., Snoke, J.A., 2001. Crustal structure beneath southern Africa and its implications for the formation and evolution of the Kaapvaal and Zimbabwe cratons. *Geophys. Res. Lett.* 28 (13), 2501–2504. <https://doi.org/10.1029/2000gl012587>.
- GEOPHYSICAL.
- Okada, Y., 1985. Surface deformation due to shear and tensile faults in a half-space. *Bull. Seismol. Soc. Am.* 75 (4), 1135–1154.
- Pollitz, F.F., Kellogg, L., Bürgmann, R., 2001. Sinking mafic body in a reactivated lower crust: a mechanism for stress concentration at the New Madrid seismic zone. *Bull. Seismol. Soc. Am.* 91 (6), 1882–1897. <https://doi.org/10.1785/0120000277>.
- Priestley, K., McKenzie, D., Debayle, E., 2006. The state of the upper mantle beneath southern Africa. *Tectonophysics* 416, 101–112. <https://doi.org/10.1016/j.tecto.2005.11.024>.
- Ranganai, R.T., Kampunzu, A.B., Atekwana, E.A., Paya, B.K., King, J.G., Koosimile, D.I., Stettler, E.H., 2002. Gravity evidence for a larger Limpopo Belt in southern Africa and geodynamic implications. *Geophys. J. Int.* 149 (3). <https://doi.org/10.1046/j.1365-246X.2002.01703.x>.
- Reeves, C.V., 1972. Rifting in the Kalahari? *Nature* 239, 73–78.
- Robert Engdahl, E., Van Der Hilst, R., Buland, R., 1998. Global teleseismic earthquake relocation with improved travel times and procedures for depth determination. *Bull. Seismol. Soc. Am.* 88 (3), 722–743. <https://doi.org/10.1130/0-8137-2349-3.461>.
- Schluter, T., 2006. Botswana. In: *Geological Atlas of Africa: with Notes on Stratigraphy, Tectonics, Economic Geology, Geohazards and Geosites of Each Country*. Springer, Berlin, pp. 46–49.
- Stamps, D.S., Calais, E., Saria, E., Hartnady, C., Nocquet, J.M., Ebinger, C.J., Fernandes, R.M., 2008. A kinematic model for the East African Rift. *Geophys. Res. Lett.* 35 (5), 1–6. <https://doi.org/10.1029/2007GL032781>.
- Stamps, D.S., Flesch, L.M., Calais, E., Ghosh, A., 2014. Current kinematics and dynamics of Africa and the East. *J. Geophys. Res., Solid Earth* 119, 1–26. <https://doi.org/10.1002/2013JB010717>.
- Vallee, M., Charlety, J., Ferreira, A.M.G., Delouis, B., Vergoz, J., 2011. SCARDEC: a new technique for the rapid determination of seismic moment magnitude, focal mechanism, and source time functions for large earthquakes using body wave deconvolution. *Geophys. J. Int.* 184, 338–358.
- Wang, X., Bradley, K.E., Wei, S., Wu, W., 2018. Active backstop faults in the Mentawai region of Sumatra, Indonesia, revealed by teleseismic broadband waveform



- modeling. *Earth Planet. Sci. Lett.* 483, 29–38. <https://doi.org/10.1016/j.epsl.2017.11.049>.
- Wang, X., Wei, S., Wu, W., 2017. Double-ramp on the Main Himalayan Thrust revealed by broadband waveform modeling of the 2015 Gorkha earthquake sequence. *Earth Planet. Sci. Lett.* 473, 83–93. <https://doi.org/10.1016/j.epsl.2017.05.032>.
- Wells, D.L., Coppersmith, K.J., 1994. New empirical relationships among magnitude, rupture length, rupture width, rupture area, and surface displacement. *Bull. Seismol. Soc. Am.* 84 (4), 974–1002.
- Weston, J., Ferreira, A.M.G., Funning, G.J., 2011. Global compilation of interferometric synthetic aperture radar earthquake source models: 1. Comparisons with seismic catalogs. *J. Geophys. Res.* 116 (B08408). <https://doi.org/10.1029/2010JB008131>.
- Weston, J., Ferreira, A.M.G., Funning, G.J., 2014. Joint earthquake source inversions using seismo-geodesy and 3-D Earth models. *Geophys. J. Int.* 198 (2), 671–696. <https://doi.org/10.1093/gji/ggu110>.
- Xie, X., Yao, Z., 1989. A generalized reflection-transmission coefficient matrix method to calculate static displacement field of a dislocation source in a stratified half-space. *Chin. J. Geophys.* 32, 191–205.
- Yang, Z., Chen, W.P., 2010. Earthquakes along the East African Rift system: a multiscale, system-wide perspective. *J. Geophys. Res., Solid Earth* 115 (12), 1–31. <https://doi.org/10.1029/2009JB006779>.
- Zhu, L., Helmberger, D.V., 1996. Advancement in source estimation techniques using broadband regional seismograms. *Bull. Seismol. Soc. Am.* 86 (5), 1634–1641. <https://doi.org/10.1785/0120160029>.
- Zoback, L., Richardson, R.M., 1996. Stress perturbation associated with the Amazonas and other ancient continental rifts stress. *J. Geophys. Res., Solid Earth* 101 (B3), 5459–5475.
- Zoback, M. Lou, 1992. First- and second-order patterns of stress in the Lithosphere: the world stress map project. *J. Geophys. Res.* 97 (B8), 11703–11728. <https://doi.org/10.1029/92JB00132>.